



HAL
open science

Topotactic fluorination of intermetallics as an efficient route towards quantum materials

Jean-Baptiste Vaney, Baptiste Vignolle, Alain Demourgues, Etienne Gaudin, Etienne Durand, Christine Labrugère, Fabio Bernardini, Andrés Cano, Sophie Tencé

► To cite this version:

Jean-Baptiste Vaney, Baptiste Vignolle, Alain Demourgues, Etienne Gaudin, Etienne Durand, et al.. Topotactic fluorination of intermetallics as an efficient route towards quantum materials. *Nature Communications*, 2022, 13, pp.1462. 10.1038/s41467-022-29043-8. hal-03616890

HAL Id: hal-03616890






<https://hal.science/hal-03616890>

Submitted on 23 Mar 2022

HAL is a multi-disciplinary open access archive for the deposit and dissemination of scientific research documents, whether they are published or not. The documents may come from teaching and research institutions in France or abroad, or from public or private research centers.

L'archive ouverte pluridisciplinaire **HAL**, est destinée au dépôt et à la diffusion de documents scientifiques de niveau recherche, publiés ou non, émanant des établissements d'enseignement et de recherche français ou étrangers, des laboratoires publics ou privés.

Topotactic fluorination of intermetallics as an efficient route towards quantum materials

Jean-Baptiste Vaney ¹, Baptiste Vignolle ¹, Alain Demourgues ¹, Etienne Gaudin¹, Etienne Durand¹, Christine Labrugère², Fabio Bernardini³, Andrés Cano ⁴ & Sophie Tencé ¹ 

Intermetallics represent an important family of compounds, in which insertion of light elements (H, B, C, N) has been widely explored for decades to synthesize novel phases and promote functional materials such as permanent magnets or magnetocalorics. Fluorine insertion, however, has remained elusive so far since the strong reactivity of this atypical element, the most electronegative one, tends to produce the chemical decomposition of these systems. Here, we introduce a topochemical method to intercalate fluorine atoms into intermetallics, using perfluorocarbon reactant with covalent C-F bonds. We demonstrate the potential of this approach with the synthesis of non-stoichiometric mixed anion (Si-F) LaFeSiF_x single-crystals, which are further shown to host FeSi-based superconductivity. Fluorine topochemistry on intermetallics is thus proven to be an effective route to provide functional materials where the coexistence of ionic and metallo-covalent blocks, and their interactions through inductive effects, is at the root of their functional properties.

¹ CNRS, Université Bordeaux, Bordeaux INP, ICMCB, UMR 5026, Pessac, France. ² CNRS, Univ. Bordeaux, PLACAMAT UMS 3626, Pessac F-33600, France. ³ Dipartimento di Fisica, Università di Cagliari, IT-09042 Monserrato, Italy. ⁴ CNRS, Université Grenoble Alpes, Institut Néel, 38042 Grenoble, France. email: sophie.tence@icmcb.cnrs.fr

A large number of topotactic reactions, preserving the architecture of the crystal lattice, have been demonstrated since the 1970s. In a topochemical phenomenon, intercalation or deintercalation of an ion is compensated by electron transfers to maintain charge neutrality. Within complex transition metal-oxide networks, this results in the reduction/oxidation of the transition elements M (mainly $M = \text{Mn, Fe, Co, or Ni}$). The intercalation of polarizing cations such as Li^+ in lamellar nickel-based oxides—from $\text{Li}_{1-x}\text{MO}_2$ to LiMO_2 ¹—or the removal of O^{2-} ions in perovskite-type networks provides two important examples widely mentioned in the literature. In the latter case, the phenomenon leads to the stabilization of infinite layers of Fe^{2+} ($3d^6$) (from SrFeO_{3-x} to SrFeO_2 ²) and also Ni^+ ($3d^9$) ions in an unusual electronic configuration (from $\text{Nd}_{1-x}\text{Sr}_x\text{NiO}_3$ to $\text{Nd}_{1-x}\text{Sr}_x\text{NiO}_2$ ³) with a well-marked two-dimensional character. Combined to thin film growth techniques, these methods applied to nickelates have recently started a new chapter in the field of superconductivity³.

In all these new compounds based on a 2D architecture, the alternation of layers whose chemical bonding harbors very different natures, are key features. In fact, the coexistence and interplay between ionic and covalent bonds together with Van der Waals forces emerge as the common thread among these systems where topochemical reactions occur. One illustration of it is the so-called inductive effect⁴, according to which the more covalent the chemical bonding within the covalent layers, the more ionic character the bonds between these layers. Thus, the topochemical approach allows not only to obtain novel compounds with new types of functional blocks but also to fine-tune some of their physical properties by playing with the nature of the chemical bonds. In fact, most of these topotactic systems exhibit mixed ionic-electronic conductivity. However, to obtain novel materials by directly stacking layers of ionic and metallic (or covalent) character remains a fundamental challenge.

Intermetallics is an important family of materials that naturally involves metallic and covalent bonding. Layered intermetallics are especially good candidates to design new compounds via this topochemical strategy by intercalating the appropriate species (element or molecule). However, when considering ionic and covalent bonds in halides, oxides, or chalcogenides where topochemical reactions assisted by redox phenomena take place, intercalation process is more difficult to handle in intermetallics which harbor extensive electronic delocalization. Among possible intercalated species, the strongly electronegative fluoride anion stands as an interesting candidate to promote novel properties in the overall structure, owing to its ability to alter chemical bonding through inductive effects and thereby creating ionic blocks. Fluorine insertion, however, has remained a challenge in intermetallic compounds. Unsuccessful attempts⁵ are ascribed to chemical decomposition caused by the over-reactivity of the hard base F^- anion on hard acid cations according to Pearson's theory. Yet, overcoming this challenge would open the door to the coexistence of metallic-covalent and highly ionic blocks within the same structure, thereby promoting a new class of materials with potentially new electronic properties (Fig. 1).

Here, we introduce a topotactic fluorination method that enables the synthesis of fluorinated intermetallics, including non-stoichiometric single-crystals. The method is based on the use of C_4F_8 perfluorocarbon reactant whose decomposition into CF_2 radicals with high dissociation energy allows reducing sufficiently the reactivity of fluorine. F^- can then slowly diffuse through the material without decomposing it. Thus, we use this method to achieve the proof-of-principle intercalation of fluorine into the LaFeSi intermetallic compound, which yields the series of non-stoichiometric LaFeSiF_x (see Fig. 2a). In addition, we show the emergence of superconductivity across this series which thus extends the family of

Fe-based superconductors to FeSi-based materials beyond the conventional ferropnictides and chalcogenides.

Results and discussion

Topochemical synthesis of non-stoichiometric fluorosilicides and characterization. We took LaFeSi as a model system to illustrate the topotactic fluorination of intermetallic compounds. This particular system is a simple Pauli paramagnet that belongs to the rich family of 111-type layered intermetallics (RTX with $R = \text{rare earth}$, $T = \text{transition metal}$, and $X = p\text{-block element}$)⁶. As shown in Fig. 2a, FeSi layers are separated by a double layer of La atoms left with empty tetrahedral sites. Direct F intercalation into the La spacer of LaFeSi was successfully achieved by means of a mild topotactic fluorination technique that enables the controlled release of over-reactive F^- ions. Specifically, we treated the LaFeSi powder with gaseous octafluorocyclobutane C_4F_8 at 500°C . This produces a mixture of two fluorinated phases. These phases are free from LaF_3 , and have only a tiny amount of LaOF (Supplementary Figs. 1 and 2). Subsequent annealing at 500°C homogenizes the F content within the sample. Thus, we finally obtained nominally pure and well-crystallized fluorinated phases isostructural to the reference 1111 materials LaFeAsO and LaFeSiH ⁷. The corresponding X-ray diffraction (XRD) pattern is illustrated in Fig. 2b–d. When subjecting LaFeSi single crystals to the same process, well-ordered and homogeneous single crystals of LaFeSiF_x are obtained, as demonstrated by precession images of a single-crystal $\text{LaFeSiF}_{0.2}$ XRD pattern (Fig. 2c). This achievement indicates a direct fluorination of an intermetallic, both in the powder and single crystal form. The successful homogeneous diffusion of fluoride anions within the structure at medium temperature and over millimetric distances for single crystals strongly indicates ionic conduction of the fluoride anions. We recall that most of complex fluorides, adopting non-stoichiometric fluorite or tysonite-type structures for instance, exhibit high fluoride (F^-) ion conductivity at room temperature with low activation energy ($5 \times 10^{-4} \text{ S cm}^{-1}$, $E_a = 0.30 \text{ eV}$ in $\text{Ce}_{1-x}\text{Sr}_x\text{F}_{3-x}$ ⁷) which reflects a high mobility of F^- ion. The ionic conductivity is strongly affected by the concentration of fluorine vacancies and consequently by the chemical composition⁸. We note that the LaF blocks in LaFeSiF_x network derive from the fluorite-type structure.

We further demonstrated the incorporation of fluorine in LaFeSi by means of X-ray photoelectron spectroscopy (XPS, Fig. 3a) and Energy Dispersive Spectroscopy (EDS) techniques (Fig. 3b). We measured three single crystals with XPS: $\text{LaFeSiF}_{0.3}$, $\text{LaFeSiF}_{0.1}$, and LaFeSi (the exact F amount is determined from the linear relationship between the F content x and the c -axis parameter for $x > 0.09$, as shown later by the analysis of single-crystal XRD data). As shown by EDS analysis on $\text{LaFeSiF}_{0.3}$, the four elements are clearly homogeneously distributed within the crystals. Besides, upon etching of the surface, we obtained an XPS signal more representative of the bulk at $\text{La } 3d$, $\text{Fe } 2p$, $\text{Si } 2s$, and $\text{F } 1s$ energy ranges. The $\text{F } 1s$ peak appears clearly $\sim 685 \text{ eV}$ at the same energy position whatever the F content. However, the intensity of the $\text{F } 1s$ peak increases from $\text{LaFeSiF}_{0.1}$ to $\text{LaFeSiF}_{0.3}$ compounds as well as the FWHM (Full Width at Half Maximum) value, associated to the heterogeneous distribution of the fluorine atoms in LaF sheet. The binding energy of the $\text{F } 1s$ differs from the energies typically observed in LaF_3 and LaOF (respectively 687 eV ⁹ and 684 eV ¹⁰), once again confirming the bulk character of the F insertion. Furthermore, the energies and shapes of the $\text{La } 3d_{5/2}$ main peak $\sim 835 \text{ eV}$ and the satellite peak $\sim 838 \text{ eV}$ strongly change upon fluorine insertion. The relative intensity of the satellite peaks depends on the orbital overlap between La atoms and its ligand atoms (F and Si). We ascribe the large

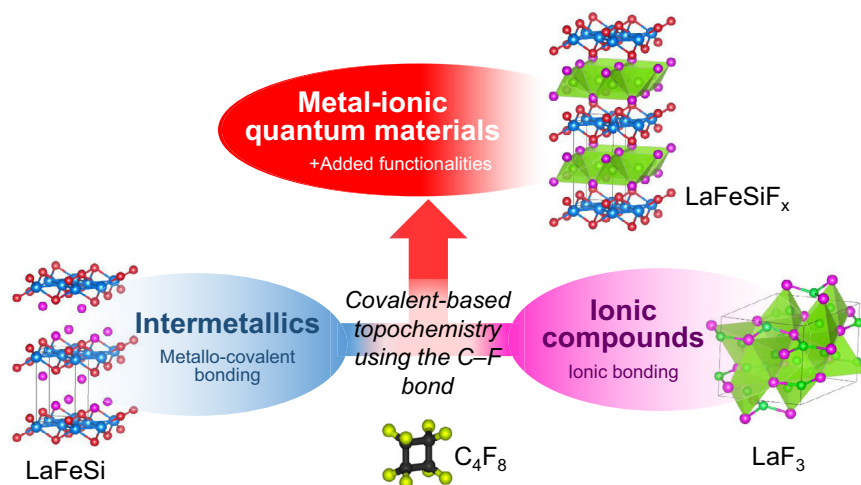


Fig. 1 Chemical synthesis strategy. Strategy to provide metal-ionic compounds based on topochemical reaction of perfluorocarbon reactant on an intermetallic compound as a host.

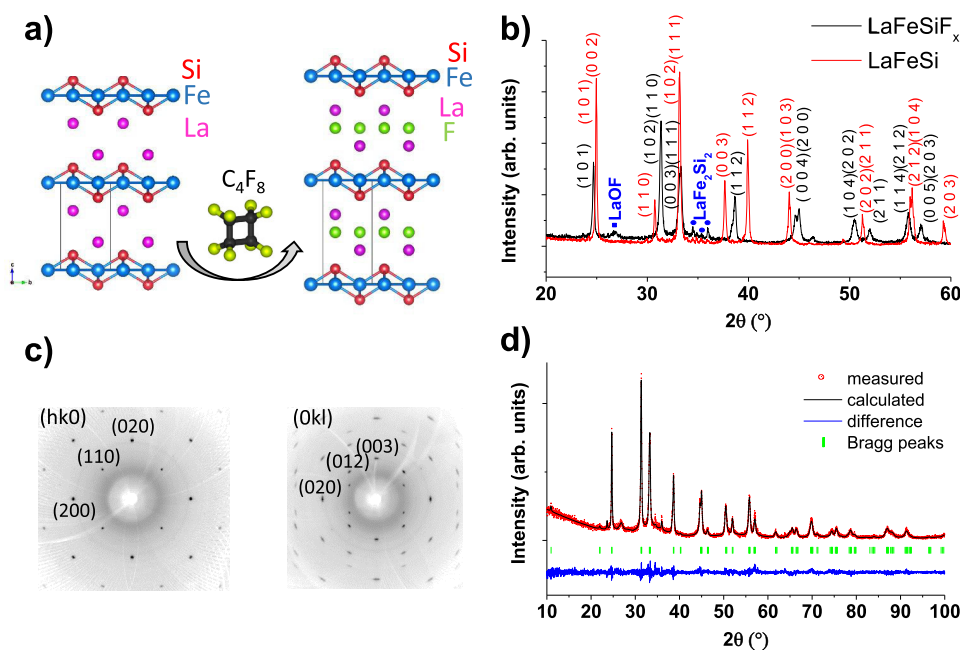


Fig. 2 X-Ray diffraction. **a** Illustration of the LaFeSi fluorination upon C₄F₈ treatment, after which the F atoms are inserted into the 2b Wyckoff positions of the *P4/nmm* structure. **b** Indexed powder X-ray diffraction patterns of LaFeSi (*a* = 4.11 Å, *c* = 7.16 Å) and LaFeSiF_x (*a* = 4.03 Å, *c* = 8.09 Å). The successful fluorination of the LaFeSi intermetallic is clearly evidenced through the shift of the Bragg peaks position. **c** Indexed precession images of the single-crystal X-ray diffraction pattern of a 50 × 50 × 10 μm³ LaFeSiF_{0.2} crystal (*a* = 4.05 Å, *c* = 8.11 Å) corresponding to (hk0) and (0kl) family planes of the reciprocal space. **d** Rietveld refinement of the LaFeSiF_x powder sample. All structural parameters were refined except the F content *x* whose accuracy is not sufficient from powder data.

increase in intensity of the satellite and its energy shift relative to the main peak upon F intercalation to a more pronounced overlap between La and Si atoms, given that the binding energy of the F1s remains constant^{11,12}. Finally, on the Si2s and Fe2p_{3/2} sides, a clear decrease of binding energy is evidenced after F incorporation, thereby illustrating an enhancement of the covalency of the global Fe-Si chemical bonding. Such analysis reveals valuable information showing that after topochemical fluorination orbital overlapping within FeSi block and that involving La-Si chemical bonding both increases noticeably. While the covalent character increase in the FeSi sheet was clearly expected, due to the inductive effect caused by the ionicity of the LaF block, the same effect observed for the La-Si bond was

somewhat unexpected but can still be ascribed to the influence of the ionic La-F bond. The creation of a low content of La-F ionic bonds (10% occupancy in the Td site of La) enhances the sharing electrons around the most polarizable anion Si involved in more covalent bond with polarizable La and polarizing Fe.

Reactional mechanism. In addition, we also treated both LaFeSi and LaFeSiH with several conventional fluorinating agents (F₂, NH₄F, KF, CF₄, PVDF...), but none of these methods (or high-temperature direct synthesis) yielded LaFeSiF_x, nor avoided the formation of the very stable ionic binary fluoride LaF₃ (Supplementary Figs. 3–8). This emphasizes the efficiency of our

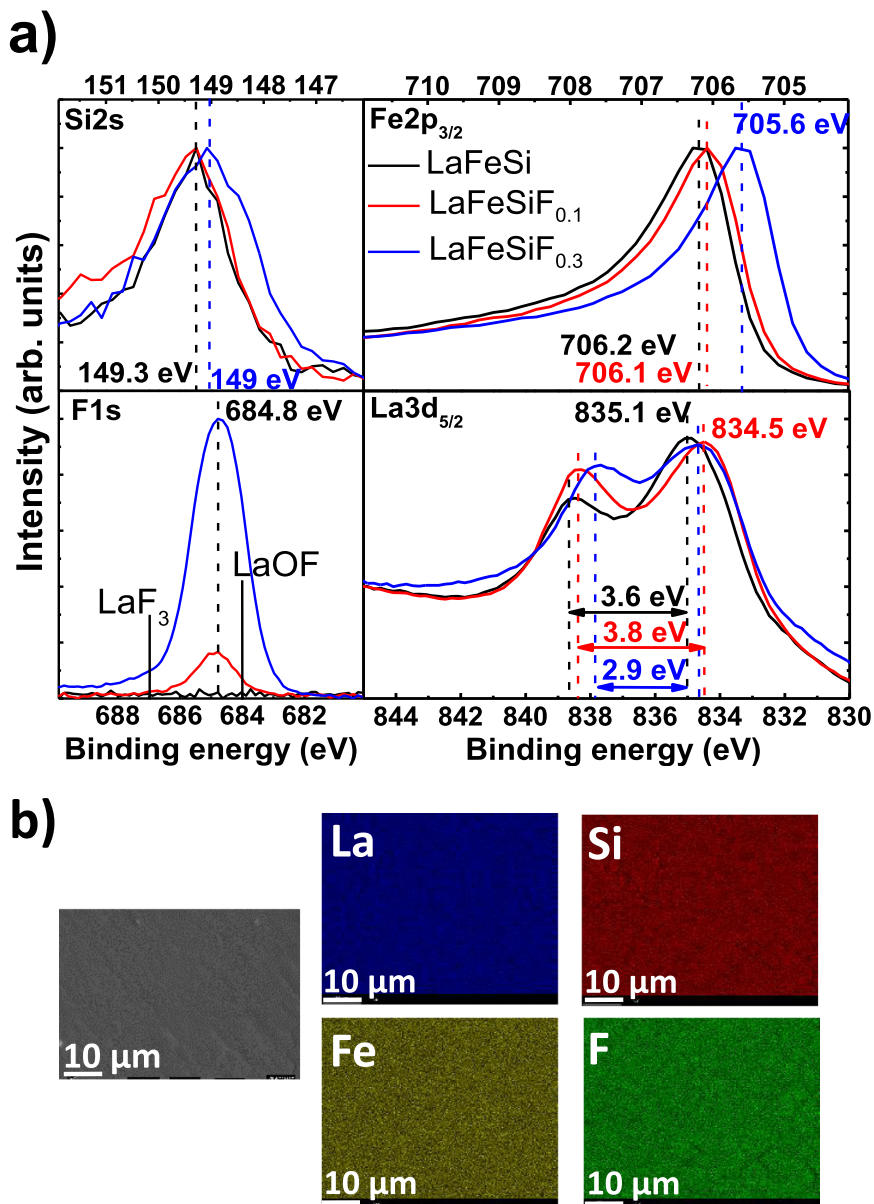


Fig. 3 X-Ray photoelectron spectroscopy. **a** XPS signals on the surface for LaFeSiF_x (x = 0, 0.1, 0.3) single crystals, for the Si2s F1s, Fe2p_{3/2}, and La3d_{5/2} core shells. The photoemission signals were acquired after several etching steps up to ~100 nm depth. **b** Secondary electron picture of the surface of a single-crystal LaFeSiF_{0.3} and corresponding La, Fe, Si, and F distribution maps for the same spot as determined by EDS analysis. The probed depth of the crystal is typically 1 μm.

fluorination route with *c*-C₄F₈. We also obtained similar results on powder with the use of polytetrafluoroethylene (PTFE) precursor (but with significant LaF₃ amount) (Supplementary Fig. 9). This suggests a tentative reaction mechanism at play between LaFeSi and *c*-C₄F₈, as PTFE thermally decomposes into the same radicals as this gas¹³. *c*-C₄F₈ is a perfluorocarbon gas mostly relevant in its use in surface treatment in the semiconducting industry, or for its insulating properties¹⁴. In our case, the effectiveness could lie in the decomposition of the cyclic perfluorocarbon, first into tetrafluoroethylene molecules C₂F₄ at 500 °C and later into difluorocarbene (:CF₂) radicals¹⁵, as observed locally in *c*-C₄F₈ plasma treatments on Si¹⁶. These electron-deficient :CF₂ radicals, presenting an unfilled *p* orbital, should naturally be attracted towards the electron-rich LaFeSi. An adsorption reaction of CF₂ radicals combined to their high dissociation energy (210 kcal/mol¹⁷ compared to 40 kcal/mol for F₂) kinetically allows for a slow release of F⁻ ions and their

subsequent diffusion into the structure. In this view of the mechanism, fluorocarbon reactants or elemental carbon should also appear as co-products. Although we were not able to identify fluorocarbon co-products, X-ray photon spectroscopy provided a spectrum for the 1s levels of carbon (Supplementary Fig. 13) suggesting the presence of graphene-like layers of carbon on the LaFeSiF_x surface after treatment.

Structural analysis. We determined the LaFeSiF_x crystal structure from the XRD data. The F-site occupancy, in particular, depends on the growth conditions and was accurately determined from single-crystal XRD refinements for selected samples (see Supplementary Tables 1 and 2). Although refining the occupancy of a partially occupied F site may seem unaccurate, the analysis of the difference-Fourier maps after refinement without fluorine shows clearly a peak in the 2*b* Wyckoff position even for x = 0.09. The

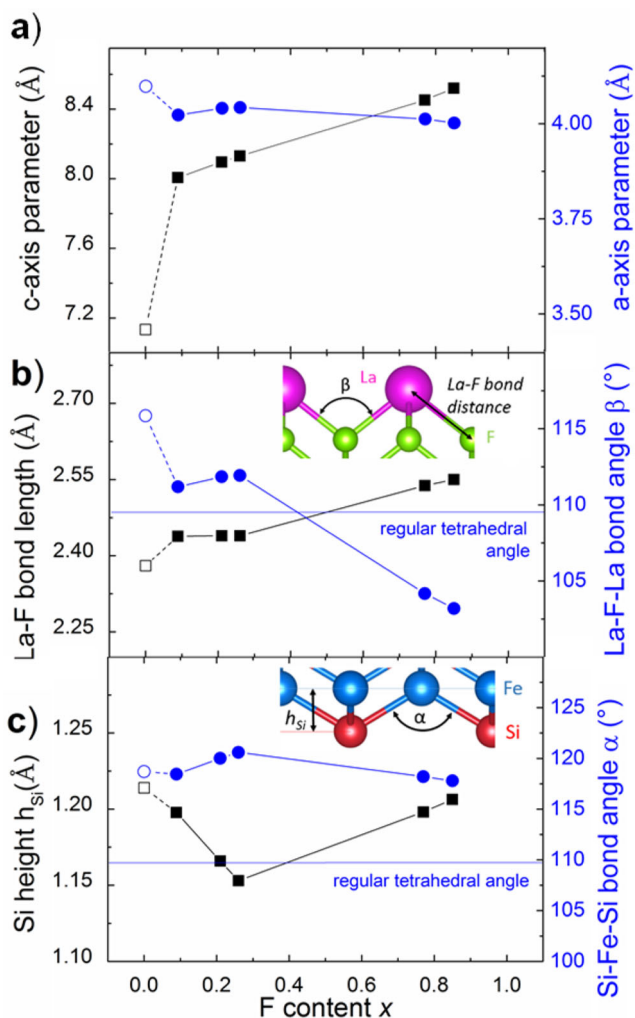


Fig. 4 Structural parameters evolution upon fluorine insertion. **a** Evolution of the a-axis and c-axis parameters versus fluorine site occupancy, from single crystals refinements. The parent compound LaFeSi is also included. Although the fully occupied sample LaFeSiF was not directly obtained, we estimate its c-parameter at 8.64 Å by extrapolation. **b** Evolution of the La-F bond distance and the La-F-La bond angle, as a function of fluorine content (single crystals X-ray diffraction data). **c** F content dependence of the anion height h_{Si} above the Fe plane and of the Si-Fe-Si tetrahedral angle α . In the insets of **b** and **c**, the definition of the h_{Si} and angle parameters discussed in the **b** and **c** graphs are given.

strong localization of the density may explain why we successfully refined the occupancy factor of fluorine position for low content values. Figure 4a shows the dependence of the c-axis parameter to the fluorine content. Strikingly, a fluorine intercalation as low as 9% produces a jump in the c-axis parameter with a +12% variation —i.e. the same c-parameter variation of LaFeSi vs LaFeSiH. The c parameter then further increases linearly as a function of the F content x . The possibility of having non-stoichiometric compositions as well as the enhanced c-axis variation both result from electrostatic and steric effects of fluoride ion. On one hand, the hard fluoride ions act as strong pillars such that only few of them are necessary to stabilize the crystals (in contrast to the softer H ions, for example, which seem to require full occupancy^{6,18}). On the other hand, as a consequence of the inductive effect, the more the ionic character of the LaF blocks, the more the covalency of the FeSi brick, leading to move away the two slabs. In that sense, the increase in the c-axis parameter is

mostly governed by the F⁻ content through the charge transfer between the two groups of layers.

Figure 4a also shows a-axis parameter as a function of x , whose relative variation is much weaker compared to c . The La-F distance, in its turn, clearly reveals two different behaviors above and below $x \sim 0.26$ (see Fig. 4b). These two regimes can also be noticed in the rest of structural parameters, including a . These variations can be ascribed to the non-monotonic deformations of the La tetrahedron induced by F intercalation and are driven mostly by steric constraints. In LaFeSi, the distance between La atoms and the center of the tetrahedron is roughly 2.39 Å and therefore F anions can barely be accommodated without enlarging the cell (the lowest distance in LaF₃ is 2.44 Å). At low F content, there is a first regime with a nearly constant bond length (2.44 Å), followed by a higher F content regime, where the La-F bond length linearly increases. This can be understood when looking at the deformation of the tetrahedron along the F concentration increase. Supplementary Fig. 14 shows the two tetrahedral angles La-F-La between La atoms belonging to the same tetrahedron. The La₄ tetrahedra centered around F atoms tends to very slightly elongate in the a-axis direction at low fluorine concentrations. When more fluorine is intercalated, the tetrahedra distortion decreases in-plane and increases along the c-axis. Overall, the cell parameters evolution seems to depend on the balance between charge transfers involving mainly FeSi layers as well as La-Si covalent bonds (through inductive effects previously illustrated by XPS analysis) and steric effects induced by the low compressibility of the electronic cloud of the fluoride anion.

The height of the Si anion relative to the Fe plane h_{Si} and the corresponding tetrahedral angle $\alpha_{Si-Fe-Si}$ are shown in Fig. 4c. These parameters have been much discussed in relation to the superconducting properties of the FeAs-based systems¹⁹, providing optimal empirical values around 1.38 Å and 109° for h_{As} and $\alpha_{As-Fe-As}$ respectively. In LaFeSiF _{x} these values are similar to those of the analogous superconducting LaFeSiH (1.20 Å and 118.2°), but away from the optimal values found in arsenides. Once more, the inductive effects may play an important role regarding this phenomenon, combined with the differences in electronic polarizability between the Si and As atoms. Through inductive effects, the covalency of the FeSi sheet is then reinforced in LaFeSiF compared to LaFeSi. However, despite the La-F bond being more ionic than La-O, the inductive effect does not allow altering sufficiently the FeSi layer covalency compared to the Fe-As bond in LaFeAsO. The latter one therefore remains more covalent than Fe-Si because of the lower polarizability of Si and leads to a FeSi sheet slightly more shrunk along the c-axis, and eventually to a smaller h_{Si} .

Electrical and magnetic measurements and superconductivity across the LaFeSiF _{x} series. Figure 5 shows the electric and magnetic properties measured across the LaFeSiF _{x} series. Data are gained from single-crystals that are bigger than the ones used for the structural characterization above (see Methods). Figure 5a shows the in-plane electrical resistance measured in a LaFeSiF_{0.10} single crystal as a function of the temperature for different values of the magnetic field $\mu_0H \parallel c$. At 0 T, superconductivity is observed with onset T_c at 9 K. The resistance drop shifts rigidly to lower temperatures as μ_0H increases. We also found superconductivity in $x = 0.30$ and 0.70 single crystals with slightly lower onset T_c and a broader transition in the latter case (Fig. 5b, upper panel). We may attribute the broadening of the transition up to $x = 0.7$ to some spatial inhomogeneity of fluorine content within the sample.

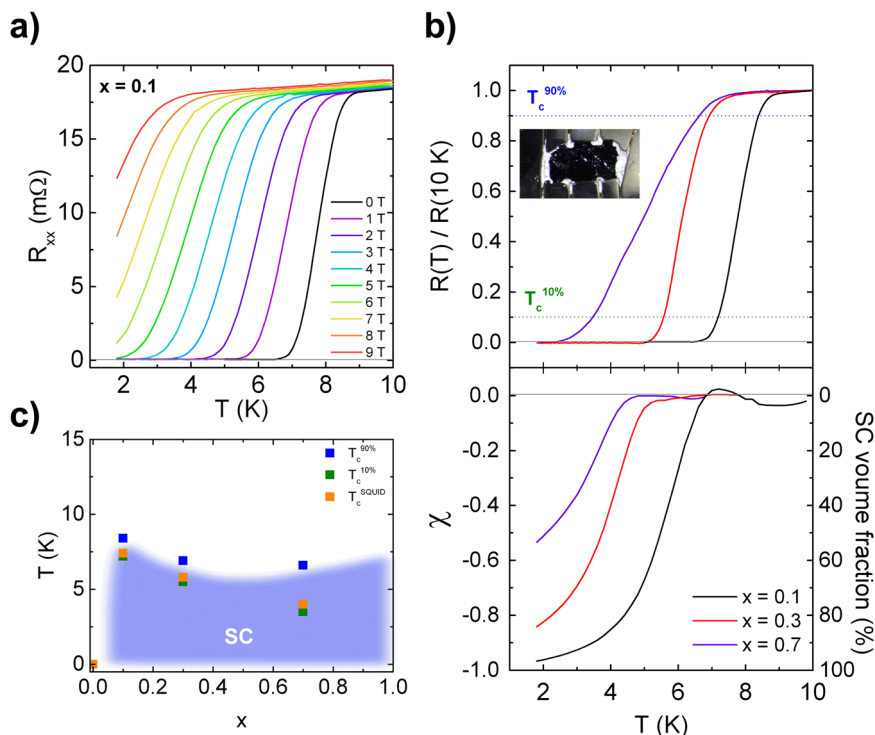


Fig. 5 Transport and magnetic measurements. **a** Temperature dependence of the electrical resistance R of the $\text{LaFeSiF}_{0.10}$ crystal at magnetic fields ranging from 0 to 9 T. **b** Upper panel: temperature dependence of the electrical resistance of the LaFeSiF_x single crystals at $x = 0.10, 0.30,$ and 0.70 normalized with respect to the resistance value measured at 10 K, with a picture of the $\text{LaFeSiF}_{0.3}$ crystal in the inset. Blue and green dotted lines represent the criteria of 90% and 10% of the normal state resistance value used to defined $T_c^{90\%}$ and $T_c^{10\%}$, respectively. Lower panel: magnetic susceptibility of the same crystals measured in zero field cooled (ZFC) conditions at 0.5 mT, with field applied along the c -axis of the crystal. The signal was corrected from demagnetizing field. **c** Temperature-composition phase diagram summarizing the superconducting transition temperatures as measured by resistivity and magnetic susceptibility.

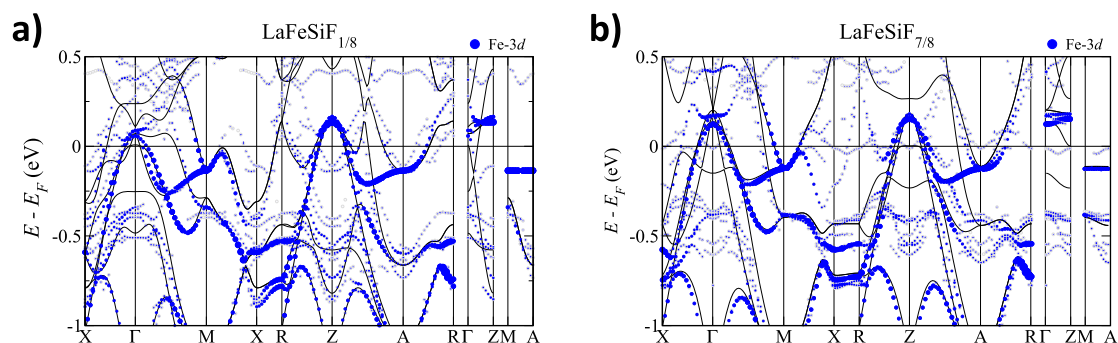


Fig. 6 Electronic structure. Electronic band structure of LaFeSiF_x along a high symmetry path in the Brillouin zone with the Fe-3d character indicated in blue. The symbols correspond to direct supercell calculations for $x = 1/8$ (**a**) and $x = 7/8$ (**b**) with the structural parameters of the $x = 0.09$ and $x = 0.85$ crystals respectively. The lines indicate the bands of the LaFeSi precursor and of the LaFeSiF end-member, computed also with the same $x = 0.09$ and $x = 0.85$ single-crystal parameters respectively. The difference between these plots reveals non-stoichiometric effects; in particular, low-energy defect-like states associated to the LaF_x spacer and consolidated vs incipient portions of the Fe-3d Fermi surface around M (also related to the specific properties of the F atom).

In addition, the Hall coefficient R_H along the LaFeSiF_x series ($x = 0, x = 0.1,$ and $x = 0.3$) has been measured (Supplementary Fig. 18) with the aim to extract the dominant type of carriers and the effective doping level. The values of R_H are positive for all samples at low temperature, indicating that charge transport is dominated by hole-like carriers in the range where superconductivity appears, in agreement with the values predicted by band structure calculation (see Supplementary Notes 4 in the Supplementary Information). The magnitude of R_H ($10^{-10} \text{ m}^3/\text{C}$) is at least one order of magnitude smaller than what is usually reported in the iron-based superconductors (IBSC) and

both the $x = 0.1$ and $x = 0.3$ fluorides harbor a strong and non-trivial temperature dependence, with a sign change of R_H occurring at 35 K (20 K) for $x = 0.1$ ($x = 0.3$). Among IBSC, these characteristics are shared by the non-magnetic FeSe superconductor, where a compensated two-band model (i.e. $n_h = n_e$) attributes the temperature dependence of R_H to a temperature dependence of the mobility of each type of carriers²⁰. We therefore conclude that the LaFeSiF_x series is best described as a compensated metal, where orbital differentiation may drive the transport properties, as proposed for the multiband Hund's metal Sr_2RuO_4 ²¹.

The lower panel of Fig. 5b shows the measured magnetic susceptibility which approaches -1 , as expected from the Meissner effect (perfect diamagnetism) in the case of $\text{LaFeSiF}_{0.1}$. While the superconducting volume fraction reaches 97% in the case of $\text{LaFeSiF}_{0.1}$, it significantly decreases for higher doping level (85% and 53% volume fraction for $x = 0.30$ and 0.70 respectively). In any case, this confirms the bulk nature of the superconductivity observed in the LaFeSiF_x series (combined to the measurement of the heat capacity in Supplementary Figs. 19 and 20 and Supplementary Notes 5), with an upper critical field H_{c2} estimated as 11.5 T for $\text{LaFeSiF}_{0.1}$ (Supplementary Fig. 22). Figure 5c displays the temperature–composition phase diagram, evidencing an extended region of superconductivity, from $x = 0.1$ to $x = 0.7$. Note that, even if the T_c is comparatively low, the robustness of such a superconducting state with respect to this type of changes in chemical composition is rather unique in the family of Fe-based superconductors.

Electronic structure upon fluorine intercalation. The insertion of F into the spacer produces an abrupt increase in the c parameter that enhances the layered character of the crystal. This structural change towards a more 2D lattice can be expected to be amplified at the electronic level due to the inductive effect. In fact, by further increasing the ionic character of the LaF_x spacer towards the $x = 1$ limit, the electronic conduction will increasingly be due to the FeSi layer in a likely 2D fashion.

Figure 6 shows the electronic structure computed for lightly (a) and heavily (b) fluorinated members of the LaFeSiF_x series. The trend obtained in these calculations confirms an increasingly 2D low-energy physics that becomes dominated by the Fe-3d states as expected from the inductive effect upon fluorination (see Supplementary Figs. 23 and 24 with a comparison with LaFeSi). For the heavily fluorinated compound, the comparison with direct supercell calculations shows that its electronic structure is essentially captured by that of LaFeSiF assuming the lattice parameters and internal atomic positions of the non-stoichiometric system. Its overall Fermi surface (FS) is indeed remarkably 2D, and much better resembles that of the reference pnictide LaFeAsO compared to the superconducting hydride LaFeSiH ^{18,22,23} (see Supplementary Fig. 24). Thus, according to the fermiology that emerges from these results, superconductivity across this series can be readily interpreted in terms of the general picture widely accepted for the Fe-based superconductors (see e.g. Hirschfeld et al.²⁴). The nesting between electron and hole FSs, however, is somewhat reduced not only because of their relative size but also due to the in-plane anisotropy of the former and non-stoichiometry effects. This is mostly detrimental for the $s \pm$ -wave pairing, yet the d -wave instability inherent to the electron FSs alone can be expected to survive²³. At the same time, we note that the superconducting T_c increases by reducing the F content while the favorable features for superconductivity are gradually washed out, and completely disappear in the non-superconducting precursor LaFeSi . This suggests a non-trivial effect of electronic correlations across the LaFeSiF_x series, which may be stronger in low F limit. In fact, according to the inductive effect, the itinerancy of the carriers within the FeSi layer can be expected to decrease with reducing the F content (in other words, metallicity in FeSi is enhanced when increasing the ionicity in the LaF_x layer). It then increases abruptly again in the non-superconducting LaFeSi precursor due its collapsed structure along c . Thus, the inductive effect, through the tuning of the La-F bond character, may provide an effective handle to control these correlations and thereby the functional properties of the system. In this respect, we note that $\text{LaFeSiF}_{0.1}$ and LaFeSiH have similar T_c 's. Following the above reasoning, this suggests a very close

behavior in terms of charge transfer and ionicity, even if the hydride has full occupancy while the fluoride 10% only.

Note again that LaFeSiF_x is related, and at the same time fundamentally different from other Fe-based superconductors such as LaFeAs(O,F) when it comes to its synthesis. Specifically, LaFeSiF_x has been obtained from the LaFeSi precursor by means of the topochemical method that we demonstrate here. Thus, by means of topochemistry, we “functionalize” the precursor and could theoretically obtain parent compounds for stoichiometric amounts of F (e.g. $x = 1$). In LaFeAs(O,F) , on the contrary, the ternary LaFeAs precursor simply does not exist, and F merely substitutes O in LaFeAsO (i.e. an already known material). Directly fluorinating an intermetallic precursor differs from the typical fluorination of ionic materials. To avoid decomposition, the fluorination reaction needs considerably less oxidizing conditions, which are very difficult to achieve with conventional methods.

In summary, we have introduced a topochemical fluorination route and demonstrated its potential for obtaining quantum materials with the synthesis of the LaFeSiF_x series. This series introduces an example of a topotactic fluorinated intermetallic compound, containing both metallic and ionic layers. Such a direct fluorine intercalation into metallic hosting structures has been remarkably elusive so far due to chemical decomposition issues. Overcoming this limitation has been possible via commercially available octacyclofluorobutane C_4F_8 and polytetrafluoroethylene. Other perfluorocarbon gases may be equally or even more effective as reactants, by playing with the covalent character of the C–F bond, which calls for further investigation. In addition, we have shown that the intercalation of fluoride anions into the structure has strong effects both on the structure and on the covalency of the FeSi layer via inductive effects. Such effects may be at the root of promoting superconductivity from LaFeSi with a F content as tiny as 9% and could explain the evolution of the properties for higher F content. Beyond this particular intermetallic, our work suggests a possible design rule to “activate” the latent functional properties of many other materials, which may span superconductivity, magnetism, mixed ionic-electronic conductivity for fluorine battery electrodes or sensors, or enhanced catalytic properties.

Methods

Synthesis. In a first step, polycrystalline LaFeSi samples, of masses between 2 and 4 g, were synthesized by arc melting in a high-purity argon atmosphere, from a stoichiometric mixture of pure elements with a La excess of 2% (Fe Alfa Aesar 99.95%, Si Alfa Aesar 99.9995%, La 99.9% Alfa Aesar). The boules were turned upside down and remelted several times to ensure chemical homogeneity. Prior to this step, pure La was pre-melted in an induction furnace for several minutes to evaporate volatile oxides and impurities. These samples were subsequently ground and cold pressed into pellets then annealed in evacuated quartz tubes for 10 days at 950 °C.

Hand-ground powders were then placed in a Pt boat inside a tubular Pt furnace and heated by induction to 500 °C for 1–4 h in a 1 bar static atmosphere of (C_4F_8 standard, Air liquide) or in the same atmosphere with a C_4F_8 flow of $10 \text{ mL} \cdot \text{min}^{-1}$ (details of the set-up are given in the Supplementary Fig. 25 of the supplementary materials). The obtained black powders were further ground, pelletized and annealed for 10 more days at 500 °C in vacuum to promote diffusion of the fluorine atoms and ensure their homogenization within the La-La layers. Cell parameters of the final compound strongly depend on the synthesis conditions: especially on the treatment duration, and on the nature of static or dynamic atmosphere.

Plate-like single crystals of LaFeSi were grown from natural cooling of an off-stoichiometric melt of composition $\text{La}_{3.5}\text{Fe}_{3.5}\text{Si}_{3.0}$ after arc melting. As-grown crystals with size ranging from $300 \times 300 \mu\text{m}^2$ to $1 \times 1.5 \text{ mm}^2$ were then subjected to the same fluorination and annealing steps described above for powders, resulting in 20–30- μm -thick brittle blackish platelet-like crystals.

In addition, fluorination treatment of the powders with polytetrafluoroethylene (PTFE, Sigma Aldrich) was carried out by mixing the appropriate amount of PTFE and base LaFeSi powders in a mortar, the mixture was sealed in a Pt tube in Ar atmosphere and treated at 400–700 °C for 12–72 h.

X-ray diffraction

Powder. X-ray powder diffraction patterns were acquired using a PANalytical X'Pert Pro diffractometer (Cu-K α radiation). The patterns were scanned over the

2θ angular range 8–100°. For each sample, we performed Rietveld refinements (with the Fullprof software²⁵) to extract the structural parameters.

Single crystals. On the basis of their shape, several small ($<40 \times 40 \times 10 \mu\text{m}^3$) single crystals were selected in the fluorinated samples upon the breaking of larger crystals. Data collection was performed using a Bruker Kappa Apex II diffractometer (Mo radiation) at room temperature. After the cell orientation-matrix searching procedure, data collection was performed at room temperature on the single crystals with the best quality of the intensity spots. Numerical absorption correction using the shape of the crystal (face indexed with the help of the video microscope) was made with SADABS-2014/5 software. All refinements were performed with the Jana2006 program package²⁶. The structure was refined with the space group $P4/nmm$ starting from the positions of the pristine compound LaFe-SiH with F replacing H at the 0.25, 0.75, 0.5 position. Details of data collections and structure refinement can be found in the crystallographic information file (CIF) deposited in the Cambridge Crystallographic Data Centre with Deposition Number CSD 2051682-2051686. All structural parameters are given in Supplementary Tables 1 and 2. Fluorine content determination for the larger crystals was obtained from the linear relationship unveiled between the c -axis parameter and the F content when refining the small crystals.

X-ray photoelectron spectroscopy. XPS surface analysis were performed using a Thermo-Fisher Scientific K-ALPHA spectrometer with a monochromatized Al K α source ($h\nu = 1486.6 \text{ eV}$) and a 200- μm X-Ray spot size. A pressure of 10^{-7} Pa was reached in the chamber when transferring the crystals. The full spectra (0–1100 eV) were obtained with a constant pass energy of 200 eV and high-resolution spectra (i.e. F1s, La3d, Fe2p, Si2s) at a constant pass energy of 40 eV. Charge neutralization was applied during analysis and subsequent etching was achieved through low-energy Ar⁺ ions. High-resolution spectra were quantified using the AVANTAGE software provided by Thermo-Fisher Scientific (Scofield sensitivity factors applied).

Transmission electron microscopy and electron diffraction. Electron diffraction experiments and the reconstruction of reciprocal space were carried out on a JEOL 2100 microscope, equipped with a double tilt specimen stage, operating at 200 kV. The powder was suspended in ethanol and a few drops of this was placed on a carbon-coated copper grid and air-dried before observation.

Magnetic measurements. The magnetic susceptibility measurements were performed on single crystals with typical dimensions of $500 \times 200 \times 20 \mu\text{m}^3$ in Zero Field Cooled (ZFC) mode at 0.5 mT using a Superconducting Quantum Interference Device (SQUID) magnetometer (MPMS XL, Quantum design). The single crystals used for the SQUID measurements are the very same samples as those used for the resistance measurements (including the quartz support and electrical gold leads, see below).

Additional measurements were performed on powdered samples with masses ranging between 10 and 20 mg. The samples (powder and single crystals) were placed in plastic capsules fixed inside a plastic straw (whose magnetization is negligible compared to that of the samples), at the appropriate position for centering with respect to the magnetic coils. For ZFC measurement, the sample is first cooled at zero magnetic field down to the lowest temperature 1.8 K. A magnetic field is then applied (along the c -axis in the cases of single crystals), and the magnetization of the sample is measured, either in a fixed magnetic field with increasing temperature ($\chi(T)$ measurements), or at a fixed temperature with increasing magnetic field ($M(B)$ measurements). The magnetic susceptibility data have been corrected for the demagnetizing factor.

Electrical measurements. The electrical transport properties were measured over a wide range of temperatures and magnetic fields up to 9T using a physical properties measurement system (PPMS, Quantum Design, using the resistivity option for compacted powders and the AC transport option for single crystals). Powder samples were compacted into 1 mm thick and 3 mm diameter pellets. Silver wires were contacted using silver paste (Dupond 4929) onto the sample surface in the aligned four-point probe configuration, and measured with a 1 mA current. Single crystals with typical dimensions of $500 \times 200 \times 20 \mu\text{m}^3$ were contacted using 20 μm gold wires and silver paste (Dupond 4929) to measure the sample resistance using a standard four points method. AC resistivity measurements were performed using currents ranging from 10 μA to 1 mA, at a frequencies ranging from 10 Hz to 300 Hz, for magnetic fields up to 9T applied along the c -axis of the crystals. The Hall coefficient R_H has been extracted by measuring the off-diagonal term of the resistivity tensor ρ_{xy} through field sweeps between -9T and $+9\text{T}$, with an excitation current up to 1 mA. The data have been anti-symmetrized to remove any contamination from ρ_{xx} due to a slight misalignment between the voltage contacts. The odd component has been extracted as $\rho_{xy} = (\rho(+B) - \rho(-B))/2$.

Heat capacity measurements. Heat capacity measurements at zero magnetic field were performed using a standard relaxation technique, as implemented in our experimental setup (PPMS, Quantum Design). As the single crystals studied in this

work were too small, with a typical mass of 30–100 μg , we have conducted heat capacity measurements on compacted powder sample, with a mass of 20–30 mg. The sample was glued to the sample holder using Apiezon N-grease and the contribution of the sample holder and grease was measured just before to subtract it to the total heat capacity measurement.

Band structure calculations. The electronic-structure calculations were performed using the all-electron code WIEN2k²⁷ based on the full-potential augmented plane-wave plus local orbitals method (APW + LO). The results (main text and Supplementary Information) were obtained in the PBE generalized gradient approximation²⁸, using experimentally determined structural parameters. The local density approximation (LDA)²⁹ was also used for comparison, which yielded essentially the same results. We choose muffin-tin radii of $R_{\text{La}}^{\text{MT}} = 2.50 \text{ a.u.}$, $R_{\text{Fe}}^{\text{MT}} = 2.40 \text{ a.u.}$, $R_{\text{Si}}^{\text{MT}} = 2.00 \text{ a.u.}$, and $R_{\text{F}}^{\text{MT}} = 1.90 \text{ a.u.}$ with the cutoff $R_{\text{MT}} \cdot K_{\text{max}} = 7.0$. The band structure calculations for the stoichiometric cases were performed using a tetragonal cell ($P4/nmm$ symmetry) encompassing 2 formula units, a $16 \times 16 \times 8 \text{ k}$ -mesh was employed for the self-consistent calculation. For the non-stoichiometric compositions, a $2 \times 2 \times 2$ tetragonal supercell was used, with an $8 \times 8 \times 4 \text{ k}$ -mesh giving an equivalent sampling to the one we used for the stoichiometric compound. The band structure of the supercell was unfolded into the Brillouin zone of the primitive cell using the unfolding algorithm as implemented in the Fold2Bloch post-processing tool^{30,31}. The original Fold2Bloch was adapted to treat the unfolding of the character of the bands.

Data availability

Details of data collections and structure refinement can be found in the crystallographic information file (CIF) deposited in the Cambridge Crystallographic Data Centre with Deposition Number CSD 2051682-2051686. The authors declare that all other data supporting the findings of this study are available within the paper and its Supplementary Information file. Additional data related to this paper are available from the corresponding authors upon reasonable request.

Code availability

WIEN2k code used for DFT calculations is available at <http://www.wien2k.at/> and Jana2006 program package used for single-crystal XRD refinements is available at <http://jana.fzu.cz>.

Received: 14 June 2021; Accepted: 15 February 2022;

Published online: 18 March 2022

References

- Radin, M. D. et al. Narrowing the gap between theoretical and practical capacities in Li-ion layered oxide cathode materials. *Adv. Energy Mater.* **7**, 1602888 (2017).
- Tsujimoto, Y. et al. Infinite-layer iron oxide with a square-planar coordination. *Nature* **450**, 1062–1065 (2007).
- Li, D. et al. Superconductivity in an infinite-layer nickelate. *Nature* **572**, 624–627 (2019).
- Goodenough, J. B. & Kim, Y. Challenges for rechargeable Li batteries. *Chem. Mater.* **22**, 587–603 (2010).
- Komuro, M., Satsu, Y., Nishi, K. & Kanda, T. Curie temperature rising by fluorination for Sm2Fe17. *AIP Adv.* **3**, 22107 (2013).
- Gupta, S. & Suresh, K. G. Review on magnetic and related properties of RTX compounds. *J. Alloy. Compd.* **618**, 562–606 (2015).
- Dieudonné, B. et al. The key role of the composition and structural features in fluoride ion conductivity in tysonite Ce1-xSrxF3-x solid solutions. *Dalton Trans.* **46**, 3761–3769 (2017).
- Chable, J. et al. Fluoride solid electrolytes: investigation of the tysonite-type solid solutions La1-xBaxF3-x ($x < 0.15$). *Dalton Trans.* **44**, 19625–19635 (2015).
- De Marco, R. et al. XPS studies of the fluoride ion-selective electrode membrane LaF3: Evidence for a gel layer on the surface. *Surf. Interface Anal.* **14**, 463–468 (1989).
- Xie, Q. et al. A novel photocatalyst LaOF: facile fabrication and photocatalytic hydrogen production. *Catal. Commun.* **27**, 21–25 (2012).
- Crerar, S. J., Mar, A. & Grosvenor, A. P. Electronic structure of rare-earth chromium antimonides RECrSb3 (RE = La–Nd, Sm, Gd–Dy, Yb) by X-ray photoelectron spectroscopy. *J. Solid State Chem.* **196**, 79–86 (2012).
- Rudyk, B. W., Blanchard, P. E. R., Cavell, R. G. & Mar, A. Electronic structure of lanthanum copper oxychalcogenides LaCuOCh (Ch = S, Se, Te) by X-ray photoelectron and absorption spectroscopy. *J. Solid State Chem.* **184**, 1649–1654 (2011).
- Wall, L. A. & Michaelsen, J. D. Thermal decomposition of polytetrafluoroethylene in various gaseous atmospheres. *J. Res. Natl Bur. Stand.* **56**, 27 (1956).

14. Harnisch, J. *Reactive Fluorine Compounds BT - Reactive Halogen Compounds in the Atmosphere* (eds Fabian, P. & Singh, O. N.) p. 81–111 (Springer Berlin Heidelberg, 1999).
15. Butler, J. N. The thermal decomposition of octafluorocyclobutane. *J. Am. Chem. Soc.* **84**, 1393–1398 (1962).
16. Martin, I. T. & Fisher, E. R. Ion effects on CF₂ surface interactions during C3F8 and C4F8 plasma processing of Si. *J. Vac. Sci. Technol. A* **22**, 2168–2176 (2004).
17. Zhang, Y., Li, Y., Zhang, X., Xiao, S. & Tang, J. Insights on decomposition process of c-C4F8 and c-C4F8 /N₂ mixture as substitutes for SF₆. *R. Soc. Open Sci.* **5**, 181104 (2018).
18. Bernardini, F. et al. Iron-based superconductivity extended to the novel silicide LaFeSiH. *Phys. Rev. B* **97**, 100504 (2018).
19. Hosono, H. & Kuroki, K. Iron-based superconductors: current status of materials and pairing mechanism. *Phys. C Supercond. Appl.* **514**, 399–422 (2015).
20. Watson, M. D. et al. Dichotomy between the hole and electron behavior in multiband superconductor FeSe probed by ultrahigh magnetic fields. *Phys. Rev. Lett.* **115**, 027006 (2015).
21. Zingl, M., Mravlje, J., Aichhorn, M., Parcollet, O. & Georges, A. Hall coefficient signals orbital differentiation in the Hund's metal Sr₂RuO₄. *npj Quant. Mater.* **41**, 1–6 (2019).
22. Singh, D. J. & Du, M. H. Density functional study of LaFeAsO_{1-x}F_x: a low carrier density superconductor near itinerant magnetism. *Phys. Rev. Lett.* **100**, 237003 (2008).
23. Bhattacharyya, A. et al. Evidence of nodal superconductivity in LaFeSiH. *Phys. Rev. B* **101**, 1–6 (2020).
24. Hirschfeld, P. J. Using gap symmetry and structure to reveal the pairing mechanism in Fe-based superconductors. *Comptes Rendus Phys.* **17**, 197–231 (2016).
25. Rodríguez-Carvajal, J. Recent advances in magnetic structure determination by neutron powder diffraction. *Phys. B Phys. Condens. Matter* **192**, 55–69 (1993).
26. Petricek, V., Dušek, M. & Palatinus, L. Crystallographic computing system JANA2006: general features. *Z. fur Krist.* **229**, 345–352 (2014).
27. Blaha, P., Schwarz, K. & Madsen, G. K. H. *WIEN2K, An Augmented Plane Wave+ Local Orbitals Program for Calculating Crystal Properties* (TU Wien, Austria, 2001). Isbn 3-9501031-1-2 2, 254 (2001).
28. Perdew, J. P., Burke, K. & Ernzerhof, M. Generalized gradient approximation made simple. *Phys. Rev. Lett.* **77**, 3865–3868 (1996).
29. Perdew, J. P. & Zunger, A. Self-interaction correction to density-functional approximations for many-electron systems. *Phys. Rev. B* **23**, 5048–5079 (1981).
30. Rubel, O., Bokhanchuk, A., Ahmed, S. J. & Assmann, E. Unfolding the band structure of disordered solids: from bound states to high-mobility Kane fermions. *Phys. Rev. B* **90**, 115202 (2014).
31. Wang, L. W., Bellaiche, L., Wei, S. H. & Zunger, A. “Majority representation” of alloy electronic states. *Phys. Rev. Lett.* **80**, 4725–4728 (1998).

Acknowledgements

J.-B.V., F.B., A.C., and S.T. were funded by the French Agence Nationale de la Recherche with the IRONMAN project (ANR-18-CE30-0018-02) and S.T. and B.V. were funded by Quantum Matter Bordeaux. Authors thanks S. Buffière and F. Weill for their help with EDS and electron microscopy measurements.

Author contributions

J.-B.V., A.D., and S.T. designed the chemical research; J.-B.V. and E.D. synthesized the samples; J.-B.V. performed the powder X-Ray Diffraction measurements and analysis; J.-B.V. and B.V. performed the resistivity, specific heat, and magnetic susceptibility measurements; E.G. performed the XRD analysis on single crystals. C.L. performed the XPS measurements. F.B. and A.C. performed the DFT calculations. J.-B.V., B.V., A.D., F.B., A.C., and S.T. wrote the paper and commented on the manuscript.

Competing interests

The authors declare no competing interests.

Additional information

Supplementary information The online version contains supplementary material available at <https://doi.org/10.1038/s41467-022-29043-8>.

Correspondence and requests for materials should be addressed to Sophie Tencé.

Peer review information *Nature Communications* thanks Weiwei Xie and the other, anonymous, reviewers for their contribution to the peer review of this work.

Reprints and permission information is available at <http://www.nature.com/reprints>

Publisher's note Springer Nature remains neutral with regard to jurisdictional claims in published maps and institutional affiliations.



Open Access This article is licensed under a Creative Commons Attribution 4.0 International License, which permits use, sharing, adaptation, distribution and reproduction in any medium or format, as long as you give appropriate credit to the original author(s) and the source, provide a link to the Creative Commons license, and indicate if changes were made. The images or other third party material in this article are included in the article's Creative Commons license, unless indicated otherwise in a credit line to the material. If material is not included in the article's Creative Commons license and your intended use is not permitted by statutory regulation or exceeds the permitted use, you will need to obtain permission directly from the copyright holder. To view a copy of this license, visit <http://creativecommons.org/licenses/by/4.0/>.

© The Author(s) 2022